machines

MDPI

Article

Development of a Compact Incremental Forming Machine

Tatiana P. Resende [1,2], Gustavo P. Carmo [1,2], Daniel G. Afonso [1,2] and Ricardo J. Alves de Sousa [1,2,*]

[1] Department of Mechanical Engineering, Centre for Mechanical Technology and Automation (TEMA), Campus Universitário de Santiago, University of Aveiro, 3810-193 Aveiro, Portugal; tatianaresende@ua.pt (T.P.R.); gustavopcarmo@ua.pt (G.P.C.); dan@ua.pt (D.G.A.)
[2] LASI—Intelligent Systems Associate Laboratory, 4800-058 Guimarães, Portugal
* Correspondence: rsousa@ua.pt

Abstract: Since the beginning of the 21st century, incremental sheet-metal-forming processes, such as single-point incremental forming (SPIF), have been the subject of extensive research. The SPIF process is highlighted as an efficient and cost-effective solution for producing complex parts with different materials and scales, surpassing conventional methods and being ideal for small series and customized products. Various machines can be used to implement SPIF, such as adapted milling machines, serial robots, and dedicated machines, each with its own advantages. However, although it requires a higher initial investment, a dedicated machine offers superior performance. The objective of this project was the creation of a compact and portable dedicated machine, which included the design of suitable kinematics, a mechanical project, and numerical control. The structural design led to the optimization of the dimensions of the robot arms. Direct and indirect kinematics were analyzed. Finally, the careful selection and adaptation of components were carried out, bearing in mind the support system of the forming punch, including the selection and sizing of motors, reducers, and linear actuators. A functional early prototype was successfully built and tested.

Keywords: incremental forming; kinematics; mechanical project; processing technology

Citation: Resende, T.P.; Carmo, G.P.; Afonso, D.G.; Alves de Sousa, R.J. Development of a Compact Incremental Forming Machine. *Machines* **2024**, *12*, 86. https://doi.org/10.3390/machines12020086

Academic Editor: Gianni Campatelli

Received: 16 November 2023
Revised: 12 January 2024
Accepted: 16 January 2024
Published: 23 January 2024

1. Introduction

The constant evolution of manufacturing processes arises from the need to improve current production methods. This leads to technological advancements in the manufacturing process aimed at making it more flexible and precise and solving issues related to compliance, the quality of the produced parts, and productivity.

One technique that has been widely researched and has consistently evolved since the early 2000s is the incremental forming process, such as single-point incremental forming (SPIF) [1,2]. The range of applications is extensive, covering many different materials and geometries. In addition to its application in the field of prototyping, the SPIF process can also be used in the production of unique parts and small series. This capability has opened up new business opportunities and enabled the development of exclusive and customized products [3].

Despite being a free-form manufacturing process, SPIF has some geometric limitations. These are mainly due to its specific forming mechanics and the material's formability limitations [4]. Therefore, it is important to establish well-defined guidelines to ensure a viable design [5].

SPIF can be implemented through different equipment. The most cost-effective and straightforward solution is to adapt milling machines [6]. However, due to their design being initially oriented toward cutting operations, they may not allow for high loads, limiting the range of employable materials. Serial robots [7] are also straightforward to implement and easily available. The most obvious advantage of serial robots is their superior kinematics due to a greater number of axes, especially when compared to three-axis Computer Numerical Control (CNC) milling machines. However, the nature of serial kinematics leads to less stiff structures, limiting the maximum available loads and, consequently, the range of materials that can be

formed. Dedicated purpose-built machines have also been developed. A dedicated machine has a higher initial investment than a customized CNC milling machine, but it is specifically designed for the SPIF operation, resulting in better performance and available workloads. Examples of dedicated machines include the ones developed at Cambridge University [6], the Amino commercial machine [8], and the SPIF-A developed at the University of Aveiro [9] using parallel kinematics to ensure higher stiffness for the SPIF operation. The SPIF-A had a workspace of 500 × 500 mm with a height displacement of 400 mm [10] and a load capacity of 20 kN, and it was able to process dual-phase steels. To achieve such a workload, the machine encompassed a considerable hydraulic system with a significant size, producing significant noise. Although it had a large workspace and could shape large parts, it was rarely used for large-sized components. In academic environments, it is more common to build small parts for testing and prototyping, which eventually led to its dismantling.

In doing so, it was planned to develop a compact incremental forming machine. It would be driven by electricity and be silent and compact to allow its coexistence with 3D printers in environments where noise levels are limited. This work involved automation, applied mechanics (direct and inverse kinematics), and mechanical design. Regarding the mechanical design, it is necessary to ensure that the machine can withstand the forming forces involved in the particular forming mechanics of incremental sheet-forming (ISF) processes.

2. Project Guidelines

This project aimed to meet the fundamental need to form small and medium-sized parts, which translates to a workspace of 200 mm × 200 mm with a vertical stroke of 100 mm. Another relevant consideration when defining the machine's architecture is determining the materials to be considered and their thicknesses. In this case, the main materials will be aluminum sheets with thicknesses ranging from 0.5 to 3 mm.

The design of a machine must take into account the forces involved in the technological process. Thus, the key to designing an incremental forming machine is predicting the forces acting on the tool during the process. The force required to form the sheet depends on the material chosen and its thickness [1]. In the present project, based on previous works related to aluminum materials [11], a 3 kN compressive load and a 1 kN lateral load were considered to be acceptable limits to form a great variety of aluminum alloy sheets. Table 1 summarizes the initially set requirements for this work.

Table 1. Main project requirements.

Workspace (mm^2)	Vertical Stroke (mm)	Sheet Thickness (mm)	Sheet Material	Forming Forces (kN)
200 × 200	100	0.5–3.0	Aluminum	3 (vertical) 1 (horizontal)

2.1. Architectural Considerations

Throughout this development project, various architectural solutions were considered and studied, considering that a single-point incremental forming process requires at least three axes. After appropriate filtering, the chosen solution was the one where one axis is controlled by a lead screw, while the other two axes are controlled by a two-axis robot, specifically a planar RR-type robot. This type of robot is referred to as a D2 Delta Robot [12]. This architecture allows for an excellent balance between the forming speed and exerted force. Additionally, it enables precise control of the process.

By analyzing the possible configurations of the arms, whether in series or in parallel (Figure 1), it can be concluded that, in a serial configuration, the precision of the process is diminished as the positional error accumulates and becomes greater than in a parallel configuration. Since precision is a key factor in an SPIF process, a parallel configuration was chosen.

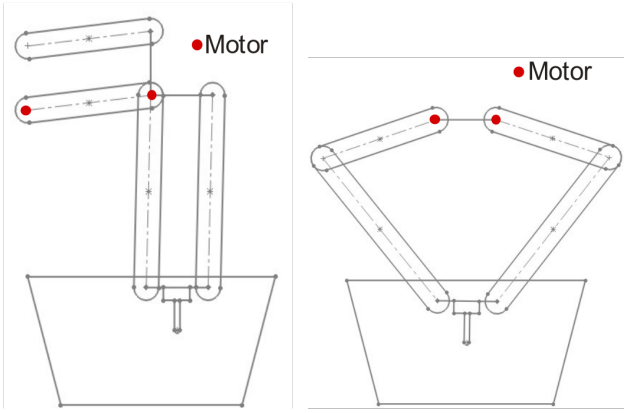

(**a**) (**b**)

Figure 1. Arm motors in (**a**) a serial configuration and (**b**) a parallel configuration.

In this configuration, the arms can be oriented in the same direction or in opposite directions, as in Figure 1b. After analyzing the torque applied to the motors, it was concluded that it is equal in both cases. The decisive factor, therefore, was the simplicity of the design with the arms oriented in opposite directions.

2.2. Optimization of Robotic Arms: Workspace and Torque Minimization

Arm optimization is an iterative process. The model is based on the premise that there are two planar RR-type arms equidistant from the center, with a distance of 45 mm. Since the developed code is intended to study torque, the implemented kinematics consider each arm separately, making it simpler. The workspace is a trapezoid with a height of 100 mm, a maximum length of 200 mm (at the top), and a wall inclined at 75 degrees.

To initiate the iterative process, the following initial values are defined: an arm length $L1$ of 120 mm and an arm length $L2$ of 150 mm. Additionally, variables for displacement in the y- and z-axes of the workspace can be considered.

The developed code (available from the authors' GitHub repository, TatianaResend) produces an output in the form of a list with 15 lines. Each line represents the torque of each motor at a specific point. The first line corresponds to the machine's origin (0, 0, 0), followed by four lines for the corners of the workspace and, finally, ten lines for internal points of the workspace.

By performing additional iterations with different initial values, it is possible to optimize the arm lengths relative to the torque, considering the workspace and realistic measurements for proper implementation.

After determining the machine's architecture, it is essential to proceed with the definition of arm lengths. This definition is subject to the workspace and the torque exerted on the motors, aiming to minimize the arm lengths without affecting the workspace or reducing the motor torque.

The motor responsible for motion along the x-axis will be positioned in the same plane as the worktable, while the other two motors, responsible for motion along the y- and z-axes, will be positioned above the work base. The height of the motors is directly related to the torque applied to them, as torque (τ) is obtained by multiplying the distance (d) between the motor and the worktable plane by the applied force (F) (as shown in Equation (1)).

$$\tau = d \times F \tag{1}$$

The optimization of arm lengths was achieved through a program developed in MATLAB. The results obtained indicate that the minimum possible lengths, without compromising the machine's structure, are 120 mm for the first arm and 150 mm for the second arm, with a distance of 290 mm between the motor and the worktable plane. Consequently, the maximum achievable torque is 665 Nm.

2.3. Kinematic Analysis

The kinematic analysis of robots is a field of study that is divided into two main parts: direct and inverse kinematic analysis. Direct kinematic analysis involves determining the motion parameters of the end-effector, such as displacement, velocity, and acceleration, based on the motion parameters of the robot's joints, such as angular displacement, angular velocity, and angular acceleration. On the other hand, inverse kinematic analysis refers to determining the motion parameters of the robot's joints based on the motion parameters of the end-effector [13].

Inverse kinematics is particularly useful in robotics for programming complex tasks like the SPIF process.

2.3.1. Direct Kinematics

As shown in Figure 2, the D2 Delta robot will be responsible for controlling the motion along the y- and z-axes. The point of interest is the midpoint of the end-effector, referred to as "O", with coordinates (Ty, Tz).

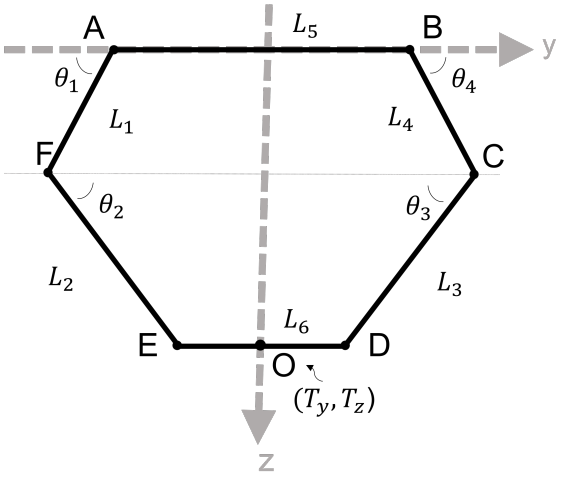

Figure 2. Diagram of the D2 Delta robot structure.

To obtain the mathematical model for the direct kinematics, we establish the relationship of motion within the system (Equations (2)–(4)) with the form

$$\begin{cases} -L_1 \cos\theta_1 + L2 \cos\theta_2 + L_6 + L_3 \cos\theta_3 - L_4 \cos\theta_4 - L5 = 0 \\ L_1 \sin\theta_1 + L_2 \sin\theta_2 - L_3 \sin\theta_3 - L_4 \sin\theta_4 = 0' \end{cases} \tag{2}$$

$$\begin{cases} T_y = -\frac{1}{2}L_5 - L_1 \cos\theta_1 + L_2 \cos\theta_2 + \frac{1}{2}L6 \\ T_z = L_1 \sin\theta_1 + L_2 \sin\theta_2 \end{cases} \text{ and} \tag{3}$$

$$\begin{cases} T_y = \frac{1}{2}L_5 + L_4 \cos\theta_4 - L_3 \cos\theta_3 - \frac{1}{2}L6 \\ T_z = L_4 \sin\theta_4 + L_3 \sin\theta_3 \end{cases}. \tag{4}$$

The coordinates of the end-effector (T_y, T_z) are obtained by rotating the angles $\theta 1$ and $\theta 4$. The relationship between θ_2 and θ_3 and θ_1 and θ_4 can be calculated from Equation (2). Thus, we obtain

$$A + B \sin\theta_3 + C \cos\theta_3 + D = 0 \tag{5}$$

where

$$A = L_1^2 - L_2^2 + L_3^2 + L_4^2 + L_5^2 + L_6^2, \tag{6}$$

$$B = -2L_1L_3\sin\theta_1 + 2L_3L_4\sin\theta_4, \tag{7}$$

$$C = -2L_1L_3\cos\theta_1 - 2L_3L_4\cos\theta_4 + 2L_3L_6 - 2L_3L_5 \quad \text{and} \tag{8}$$

$$\begin{aligned} D = &-2L_1L_4\sin\theta_1\sin\theta_4 + 2L_1L_4\cos\theta_1\cos\theta_4 - 2L_1L_6\cos\theta_1 \\ &+2L_1L_5\cos\theta_1 - 2L_4L_6\cos\theta_4 + 2L_4L_5\cos\theta_4 - 2L_5L_6 \end{aligned}. \tag{9}$$

Taking into account the equality $\sigma = \tan\frac{\theta_3}{2}$ and using the trigonometric identities, we can obtain the equation $\tan\theta_3 = \frac{2\tan(\frac{\theta_3}{2})}{1-\tan^2(\frac{\theta_3}{2})} = \frac{2\sigma}{1-\sigma^2}$. Thus, we can conclude that $\sin\theta_3 = \frac{2\sigma}{1+\sigma^2}$ and $\cos\theta_3 = \frac{1-\sigma^2}{1+\sigma^2}$.

By substituting the values of $\sin\theta_3$ and $\cos\theta_3$ into Equation (5), we obtain the following:

$$A + B\frac{2\sigma}{1+\sigma^2} + C\frac{1-\sigma^2}{1+\sigma^2} + D = 0. \tag{10}$$

Simplifying Equation (10), we obtain

$$\sigma^2(A - C + D) + \sigma(2B) + (A + C + D) = 0 \tag{11}$$

$$\sigma = \frac{-B \pm \sqrt{B^2 - (A - C + D)(A + C + D)}}{A - C + D} \tag{12}$$

$$\theta_3 = 2\tan^{-1}\sigma \tag{13}$$

$$\theta_2 = \sin^{-1}\frac{-L_1\sin\theta_1 + L_3\sin\theta_3 + L4\sin\theta_4}{L_2}. \tag{14}$$

Substituting Equation (14) into Equation (3) allows us to find the coordinates of the end-effector:

$$\begin{cases} T_y = -\frac{1}{2}L_5 - L_1\cos\theta_1 + L_2\cos\theta_2 + \frac{1}{2}L6 \\ T_z = L_1\sin\theta_1 + L_2\sin\theta_2 \\ \theta_2 = \sin^{-1}\frac{-L_1\sin\theta_1 + L_3\sin\theta_3 + L4\sin\theta_4}{L_2} \end{cases} \tag{15}$$

Substituting Equation (14) into Equation (4) allows us to find the coordinates of the end-effector:

$$\begin{cases} T_y = \frac{1}{2}L_5 + L_4\cos\theta_4 - L_3\cos\theta_3 - \frac{1}{2}L6 \\ T_z = L_4\sin\theta_4 + L_3\sin\theta_3 \\ \theta_3 = 2\tan^{-1}\sigma \end{cases} \tag{16}$$

By using Equations (15) and (16) and knowing the input angles θ_1 and θ_4, it is possible to calculate the coordinates of the end-effector (T_y, T_z).

2.3.2. Inverse Kinematics

By knowing the coordinates of the end-effector (T_y, T_z) through Equations (25) and (34), it is possible to calculate the input angles θ_1 and θ_4. The inverse kinematic analysis of the D2 Deltarobot is based on the coordinates of the end-effector (T_y, T_z), which can be used tosolve for the rotation angles θ_1 and θ_4. Using Equation (3), the following is obtained:

$$A1 + B1\sin\theta_1 + C1\cos\theta_1 + D1 = 0 \tag{17}$$

where

$$A1 = T_y^2 + T_z^2 + L_1^2 - L_2^2 + 0.25L_5^2 + 0.25L_6^2, \tag{18}$$

$$B1 = 2T_yL_1 + L_1L_5 - L_1L_6, \tag{19}$$

$$C1 = -2T_zL_1, \tag{20}$$

$$D1 = T_yL_5 - T_yL_6 - 0.5L_5L_6. \tag{21}$$

Taking into account the equality $\sigma = \tan\frac{\theta_1}{2}$ and using the trigonometric function identities, we can obtain the equation $\tan\theta_1 = \frac{2\tan(\frac{\theta_1}{2})}{1-\tan^2(\frac{\theta_1}{2})} = \frac{2\sigma}{1-\sigma^2}$. Thus, we can conclude that $\sin\theta_1 = \frac{2\sigma}{1+\sigma^2}$ and $\cos\theta_1 = \frac{1-\sigma^2}{1+\sigma^2}$. Substituting the values of $\sin\theta_1$ and $\cos\theta_1$ into Equation (17), we have

$$A1 + B1\frac{2\sigma}{1+\sigma^2} + C1\frac{1-\sigma^2}{1+\sigma^2} + D1 = 0. \tag{22}$$

Simplifying Equation (22), we obtain

$$\sigma^2(A1 - C1 + D1) + \sigma(2B1) + (A1 + C1 + D1) = 0 \tag{23}$$

$$\sigma = \frac{-B1 \pm \sqrt{B1^2 - (A1 - C1 + D1)(A1 + C1 + D1)}}{A1 - C1 + D1} \tag{24}$$

$$\theta_1 = 2\tan^{-1}\sigma. \tag{25}$$

Using Equation (4), we can obtain

$$A2 + B2\sin\theta_4 + C2\cos\theta_4 + D2 = 0 \tag{26}$$

where

$$A2 = T_y^2 + T_z^2 + L_4^2 - L_3^2 + 0.25L_5^2 + 0.25L_6^2, \tag{27}$$

$$B2 = -2T_yL_4 + L_4L_5 - L_4L_6, \tag{28}$$

$$C2 = -2T_zL_4, \tag{29}$$

$$D2 = -T_yL_5 + T_yL_6 - 0.5L_5L_6. \tag{30}$$

Taking into account the equality $\rho = \tan\frac{\theta_4}{2}$ and using the trigonometric function identities, we can obtain the equation $\tan\theta_4 = \frac{2\tan(\frac{\theta_4}{2})}{1-\tan^2(\frac{\theta_4}{2})} = \frac{2\rho}{1-\rho^2}$. Thus, we can conclude that $\sin\theta_4 = \frac{2\rho}{1+\rho^2}$ and $\cos\theta_4 = \frac{1-\rho^2}{1+\rho^2}$. Substituting the values of $\sin\theta_4$ and $\cos\theta_4$ into Equation (26), we obtain

$$A2 + B2\frac{2\rho}{1+\rho^2} + C2\frac{1-\rho^2}{1+\rho^2} + D2 = 0. \tag{31}$$

Simplifying Equation (31), we obtain

$$\rho^2(A2 - C2 + D2) + \rho(2B2) + (A2 + C2 + D2) = 0 \tag{32}$$

$$\rho = \frac{-B2 \pm \sqrt{B2^2 - (A2 - C2 + D2)(A2 + C2 + D2)}}{A2 - C2 + D2} \tag{33}$$

$$\theta_4 = 2 \tan^{-1} \rho. \tag{34}$$

By using Equations (25) and (34) and knowing the coordinates of the end-effector (T_y, T_z), it is possible to calculate the input angles θ_1 and θ_4.

3. Mechanical Design

The development of a machine requires careful attention to the components used. It is important to choose components that can be easily acquired in the market or whose manufacturing is relatively simple in order to reduce project costs. Additionally, it is essential to consider the materials used to ensure that the machine can adequately withstand the forces exerted upon it without being overly conservative. These considerations are fundamental to guaranteeing the effectiveness, efficiency, and safety of the machine while also aiming to optimize the costs and resources involved in the project.

3.1. Robotic Arm Design

The configuration of a D2 Delta robot consists of two main arms, one on the right side and another on the left side, responsible for movement and force support, accompanied by one or two secondary arms to ensure platform parallelism, as demonstrated in Figure 3a. However, for processes involving horizontal forces, such as SPIF, it is preferable to use a configuration with three main arms in a triangular arrangement, as shown in Figure 3b. This configuration significantly increases the robot's resistance to horizontal forces, providing greater efficiency.

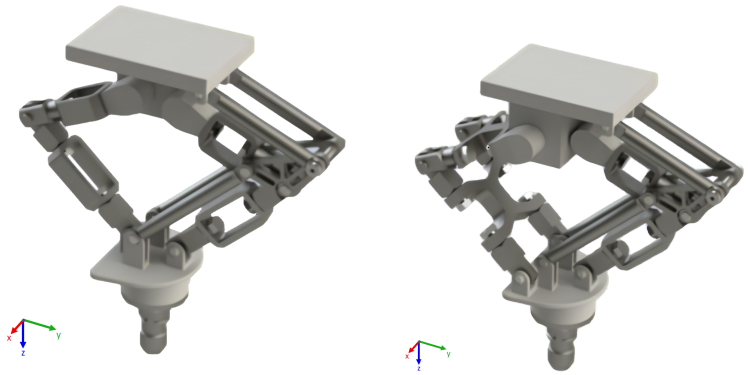

(**a**) (**b**)

Figure 3. Robot arm configurations with (**a**) two main arms and (**b**) three main arms.

Two of the three main arms are aligned relative to the *y*-axis (on the left side) and move together, while the third arm (on the right side) is equidistant on the *x*-axis from the other two arms. To ensure synchronized movement between the two arms on the left side, they are connected by "X"-shaped components, allowing not only their movement together but also easy coupling between the components. The structure of the right-side arm is in the shape of an "O", simplifying the coupling between components. On the same side, there are two secondary arms that ensure parallelism.

The movement of the platform and, consequently, the tool is ensured by the motion of motors attached to the arms at the top. The motion is transmitted through universal joints to allow torque transmission at different angles.

In situations where it is necessary to allow movement between two parts with a low load and moderate rotational speed, bushings are used. This method is considered a more cost-effective option than using bearings.

Figure 4, case (a), illustrates the assembly of the components of the main arms on the left side, and case (b) illustrates the assembly of the main arm on the right side.

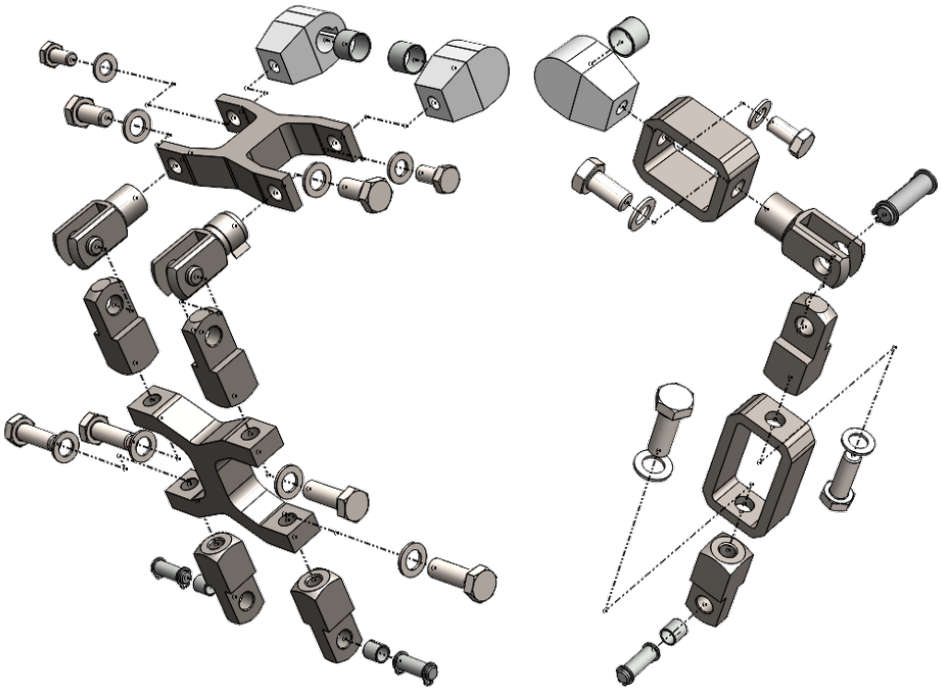

(**a**) (**b**)

Figure 4. Assembly diagram of the main arm components on the (**a**) left side and the (**b**) right side.

3.2. Support System for the Forming Punch

Given that there are forces acting on the sheet during the SPIF process, a mechanical support system has been developed and integrated into the platform to accommodate the forming punch. This approach is beneficial because it requires fewer components and simplifies assembly.

The support system has been designed to meet process requirements, ensuring minimal friction during the passive sliding of the punch on the sheet and proper integration with the machine structure.

Figure 5 illustrates the main components of the system, which include a shaft connecting the platform to the tool holder, a bearing to ensure proper positioning and support for the shaft, and a cover to position and provide access to the components.

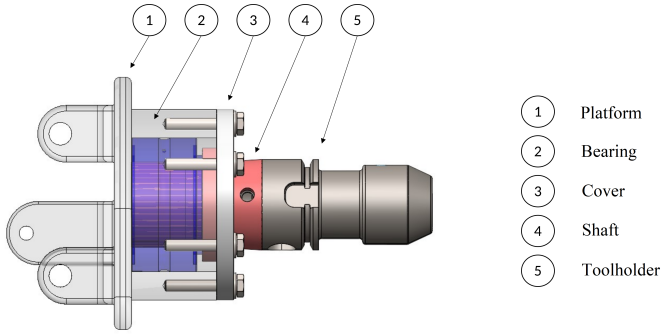

Figure 5. Components of the support system for the forming punch.

3.3. Bearing Selection

The selection of bearings follows three fundamental criteria, which include proper shaft positioning, the minimization of displacements, and resistance to process forces.

The types of bearings studied include the following:

- Needle roller bearings: These are composed of long, thin rollers that support high radial loads in limited spaces. They have a high radial load capacity but do not support much axial load.
- Single-row deep-groove ball bearings: These have a ball track and a deep groove in both the outer and inner rings to support light radial and axial loads.
- Combined needle roller and thrust ball bearings: These are a combination of needle rollers and balls to support both radial and axial loads simultaneously. They can support higher radial loads than ball bearings and higher axial loads than needle roller bearings.

In the SPIF process, which involves axial and radial loads, the combined needle roller and thrust ball bearing is the most suitable solution. The main characteristics of this bearing can be observed in Table 2.

Table 2. Main characteristics of the combined needle roller and thrust ball bearing. Adapted from SKF [14].

	Radial	**Axial**
C_0	39 kN	6.32 kN
C	25.5 kN	4.54 kN
P_u	4.65 kN	0.268 kN
Load	Flexion and compression (guidance and support)	
v_{ref}	11,000 r/min	
v_{lim}	13,000 r/min	
Mass	0.15 kg	

3.4. Tool Holder

The tool holder is a critical component, acting as a passive connection between the shaft and the forming punch, with the aim of efficiently transmitting the rotational motion of the punch to the shaft without compromising the efficiency of the connecting elements.

To ensure the proper performance of the tool holder, three points must be considered: concentricity, clamping force, and standardization. The concentricity of the rotation axes of the platform and the punch must be maintained, while the tool must be securely held to prevent its rotation or release during work, which can pose hazards. All of the different components must be consistent with each other.

Although there are various tool holders available in the market for different technological processes, the SPIF process is still relatively new, with limited development in specialized equipment. Therefore, it will be necessary to choose an existing tool holder for another technological process and adapt it to the specific needs of the SPIF process. A tool holder consists of three main elements: the cone, the flange, and the tool fixation system, as illustrated in Figure 6. The interface between the platform and the tool holder is formed by a cone, which can be of different types.

The CAT, ISO, and DIN cones are some of the many available different tool holders available [15] and represent the most prevalent and versatile types used in the industry. The housing is simple and does not have many requirements, making it ideal for prototypes and machines with manual tool changes. On the other hand, the HSK (*Hohlfutter Schaft Konus*) cone with a hollow shank is characterized by a flat cone–hole contact surface. It is especially suitable for high-speed machines due to its high balance, as well as high static and dynamic rigidity. Its centralized fixation allows for bending loads up to twice as high as common conical tool holders. The floating cone, on the other hand, is indicated for threading and

reaming operations due to the complex balance of rotational and axial movement that occurs during thread generation. However, it is not recommended for processes involving radial fluctuations, as it does not provide resistance to bending.

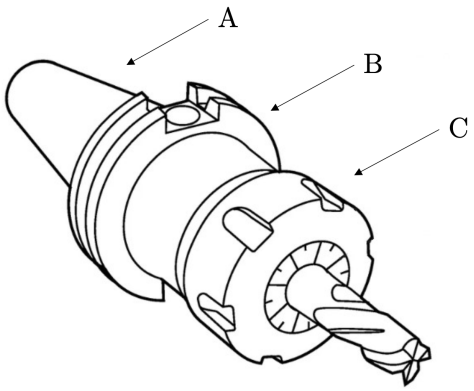

Figure 6. Tool holder assembly: A—cone; B—flange; C—tool fixation system.

The flange is a flat, circular surface located at the bottom end of the tool holder and is used to support the base of the tool to be fixed. The flange is typically attached to the cone of the tool holder, either by screws or by a mechanical locking system. In addition to serving as a point of support for the tool, it is also responsible for transmitting the cutting forces and torque generated during the workpiece forming process to the machine tool.

There are four categories of fixation systems employed to ensure tool fixation in the tool holder. The first type is the collet chuck, which uses a metal sleeve to hold the tool and is locked with a nut. The second type is the hydraulic chuck, which uses an oil reservoir to balance the clamping pressure. The third type is the shrink-fit chuck or thermal clamping, which utilizes a heater to expand the bore into which the tool is inserted and then cools down to firmly hold the tool. The fourth type is the Weldon chuck, which uses a radial screw to hold the tool, requiring a flat area on the shank. To properly meet the demands of the SPIF process, the most suitable option is to use a tool holder with an HSK cone shape in combination with a Weldon chuck. This combination offers high clamping rigidity and is easy to handle, even for operators without specific expertise. Figure 7 shows an example of this type of tool holder.

Figure 7. Selected tool holder: HSK cone with a Weldon chuck. Adapted from Sanches Blanes [16].

3.5. Selection and Sizing of the Motor–Reducer Assembly

To meet the maximum required torque of 665 Nm, it is crucial to properly size and select both the motor and the gearbox. This selection is essential to ensure the performance and efficiency of the system, as well as the safety of the operating environment. This implies

that the motors should have the power to execute all commands sent by the controller, even if the torque increases. To meet this requirement, the use of a closed-loop motor is recommended, which includes an encoder, coupled to the shaft. The encoder sends a feedback signal to the controller indicating the actual displacement of the shaft. Thus, the controller can continuously monitor whether the motor is correctly positioned and take action if any changes occur.

Based on this premise, Fernandes [17] conducted a study on various types of motors for application in the SPIF process, namely, servo motors, brushless DC motors, and stepper motors. Given the need to work with low speeds and high torques, it was concluded that stepper motors offer the best cost–benefit ratio. After a careful analysis of the various options, the chosen motor for the project in question was the NEMA 34. This motor exhibits excellent performance in terms of torque and precision, and it also has a size compatible with the project's requirements. The main features of this motor are presented in Table 3.

Table 3. Main characteristics of the NEMA 34 motor.

Number of phases	2
Holding torque	12 Nm
Rated current per phase	6.0 A
Phase resistance	0.72 ohms
Inductance	7.3 mH ± 20% (at 1 kHz)
Frame size	86 × 86 mm
Body length	150.6 mm
Shaft diameter	∅ 14 mm
Shaft length	37 mm
Key length	25 mm
Number of connections	4
Cable length	270 mm

Considering a maximum torque of 665 Nm, the chosen motor for the system has a torque of 12 Nm, requiring the use of a gearbox with a theoretical transmission ratio of 56:1. For this purpose, planetary gearboxes were evaluated, including spur-gear and helical-gear planetary gearboxes, as well as precision worm gearboxes. Precision worm gearboxes have relatively low efficiency compared to spur and helical gears, which can be a disadvantage in applications that require high efficiency [18,19]. Given the need for significant force application in the SPIF process, the selection of a low-efficiency gearbox, such as a worm gearbox, could result in a significant reduction in torque transmission efficiency. Additionally, worm gearboxes tend to generate more heat due to the friction between the worm screw and the worm gear. Thus, the use of worm gearboxes was excluded, with the focus going to the analysis of spur-gear and helical-gear gearboxes.

Study of the Motor–Reducer Configuration

Throughout the entire machine development process, it was crucial to consider compatibility requirements, resulting in a study to select the motor–reducer configuration. The first approach, depicted in Figure 8, is to position the motor vertically and use a 90-degree reducer. This configuration offers the advantage of not needing a transmission system between the reducer shaft and the arms, resulting in higher efficiency and cost savings. However, this configuration is not favorable, as it requires an adaptation of the access area to the worktable.

The second hypothesis, represented in Figure 9, positions the motor horizontally at the top of the structure and uses a linear reducer. This configuration is compact and does not have the disadvantage of the previous configuration. However, this configuration requires a transmission system, resulting in higher cost and lower efficiency.

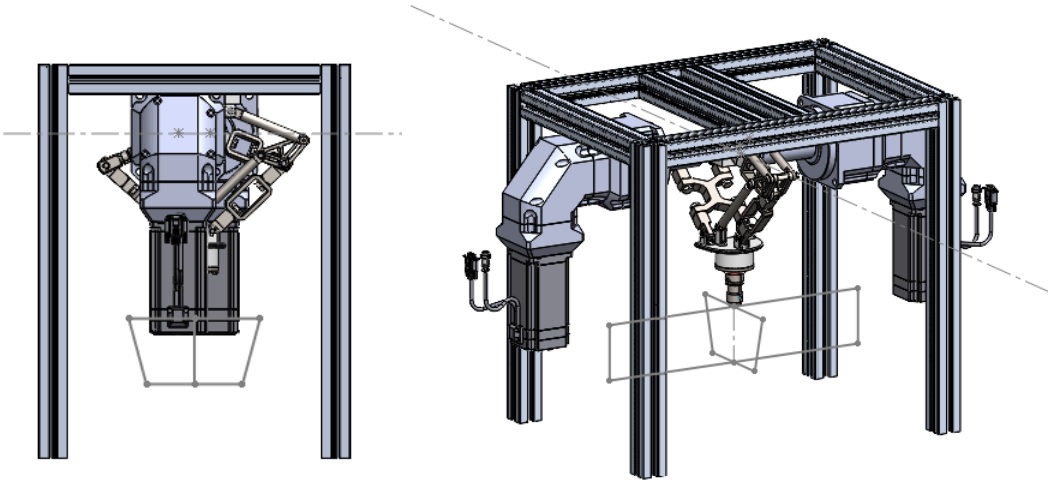

Figure 8. Hypothesis 1 motor–reducer configuration: vertical motor with a 90-degree helical reducer.

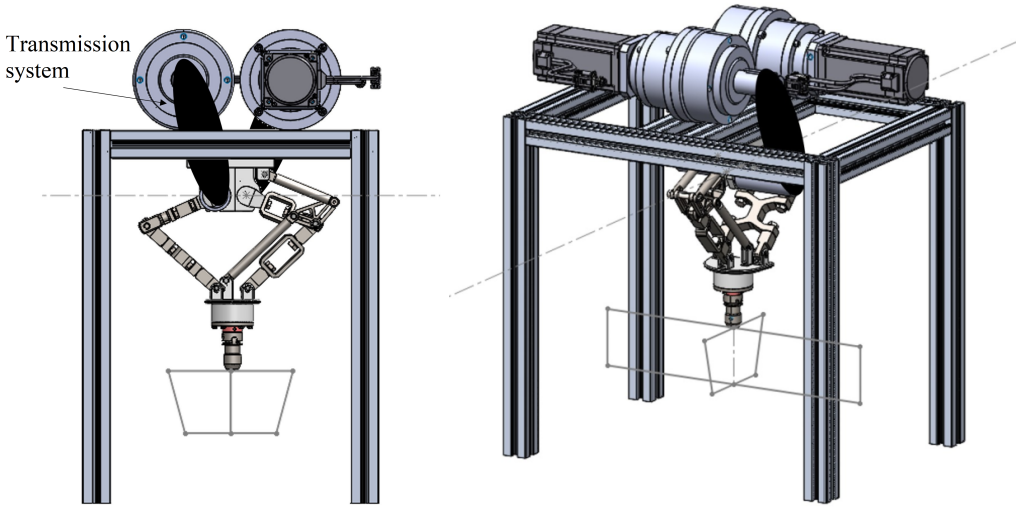

Figure 9. Hypothesis 2 motor–reducer configuration: motor positioned horizontally at the top of the structure with a linear reducer.

In hypothesis 3, the motor–reducer configuration positions the motor horizontally and uses a 90-degree reducer. The system is compact, although the motor is not fully enclosed by the structure. It does not interfere with the access to the worktable and does not require a transmission system, overcoming the disadvantages of the previous configurations. Another configuration studied, presented in Figure 11, positions the motor horizontally and uses a linear reducer. This configuration offers the same advantages as hypothesis 3.

In summary, hypotheses 3 and 4, represented in Figures 10 and 11, respectively, are nearly equivalent, with the difference between them possibly being the price of the reducer.

Initially, based on the theoretical torque value of 665 Nm, which corresponds to a reduction ratio of 56:1, alternatives available in the market were examined from various suppliers. After careful analysis, it was found that straight-gear reducers faced difficulty in achieving such high torque values. In line with the torque reduction premise, three helical reducers were found, with a reduction ratio of 60:1 and a torque of 600 Nm. Although this is lower than the theoretical value, this torque represents the nominal torque, indicating that the maximum torque achieved by the reducer is higher, namely, up to three times higher than the nominal torque. Two out of the three reducers are 90-degree helical reducers, while the other one is a linear helical reducer. Table 4 presents the main characteristics of the analyzed reducers. The 90-degree helical reducers have a higher capacity to withstand radial loads, while linear helical reducers are more compact and perform better in high-precision applications.

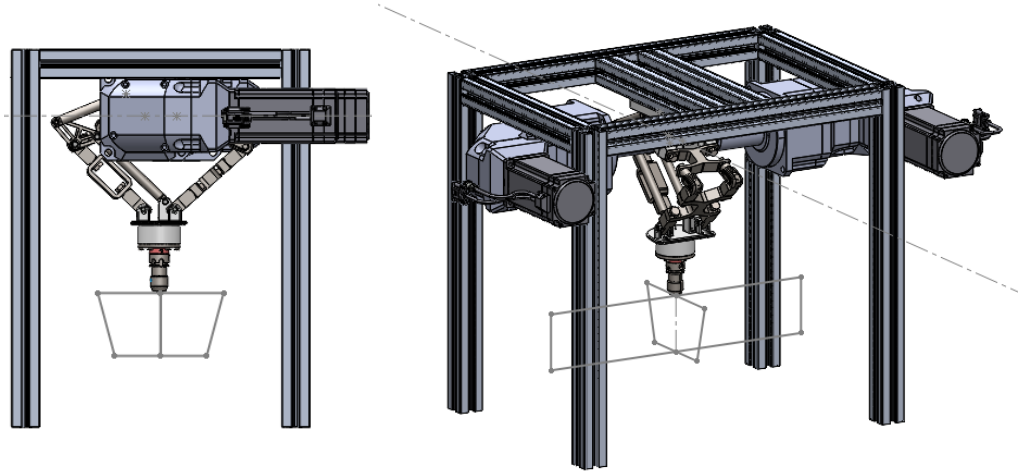

Figure 10. Hypothesis 3 motor–reducer configuration: motor positioned horizontally with a 90-degree helical reducer.

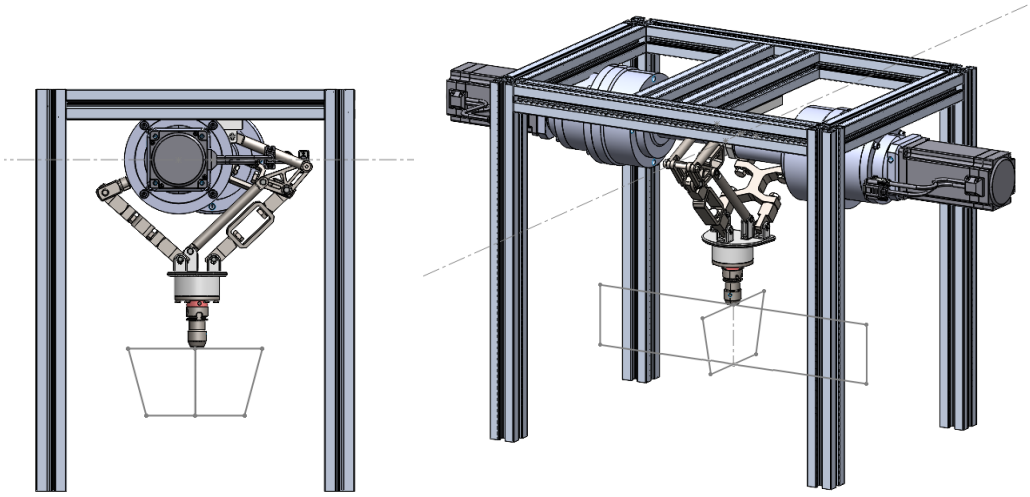

Figure 11. Hypothesis 4 motor–reducer configuration: horizontal motor with a linear reducer.

Table 4. Characteristics of the analyzed reducers.

		ABR142 [20]	**AER155 [21]**	**AE155 [22]**
Type		90 degrees	90 degrees	linear
Nominal input speed	rpm	3000	3000	3000
Nominal radial load	N	9400	8460	8460
Nominal axial load	N	4700	4700	4700
Efficiency	%	$\geq$92	$\geq$92	$\leq$94
Weight	kg	27.5	21.8	17
Length	mm	365	324.5	239
Price	EUR	3805.00	3398.00	2237.00

After a comparative analysis of the reducers, the AE155 linear helical reducer was chosen following hypothesis 4, as shown in Figure 11. Although the 90-degree helical reducers have significant advantages, the linear reducer better meets the specific requirements of the application, including the limited available space, the need for high precision, and lower cost. Furthermore, the 60:1 reduction ratio with a nominal torque of 600 Nm is suitable for the application at hand. Therefore, the selection of the AE155 linear reducer was the most appropriate choice. A custom-made aluminum plate was designed to enable the fixation of the reducer to the machine frame.

3.6. Selection and Sizing of the Motor—Linear Actuator Assembly

While the motor–reducer assembly is responsible for ensuring the movement of the *y*- and *z*-axes of the machine, the motor–linear-actuator assembly is responsible for the *x*-axis. In order to standardize the components, a similar process to that described before was adopted to select the motor, resulting in the same motor choice. To select linear motion control systems, it is necessary to consider requirements such as force, speed, distance traveled, precision, repeatability, and service life. Among the types of motion control drives, the following stand out: ball-screw drives, lead-screw drives, and belt drives [23,24]. Several ball-screw and belt-drive systems were analyzed. Table 5 presents the characteristics of three linear actuators, one ball-screw and two belt drives, that meet the project requirements.

Table 5. Characteristics of the linear actuators under analysis.

		MTJ40 ECO L	**MTV40 1205**	**TLM105G**
Drive Type		Belt	Ball	Belt
Carriage Length	mm	200	150	300
Dynamic Torque	Nm	Mx = 158	Mx = 28	Mx = 76
		My = 660	My = 260	My = 296
		Mz = 660	Mz = 260	Mz = 296
Maximum Force	N	Fpy = 6540	Fpy = 2300	Fpy = 6355
		Fpz = 10,190	Fpz = 3860	Fpz = 6355
Maximum Torque	Nm	Mx = 60	Mx = 23	Mx = 168
		My = 341	My = 210	My = 679
		Mz = 219	Mz = 130	Mz = 679
Maximum Axial Force	N	262	3400	3451
Maximum Speed	m/s	3	0.49	3
Price	EUR	740.00	1156.41	1500.00

Any of the three options analyzed can meet the project requirements. By using a linear actuator with a ball-screw drive, a higher precision is achieved compared to belt-driven actuators, which is an important aspect of the SPIF process. However, due to economic considerations, the MTJ40 ECO L model was initially chosen. In the future, it is recommended to conduct a second evaluation considering the available budget for the project in order to verify whether the MTJ40 ECO L actuator remains the most suitable option.

3.7. Motor—Linear Actuator Connection

The movement of the worktable is ensured by two linear actuators, and this type of configuration is commonly known as 2x, as shown in Figure 12.

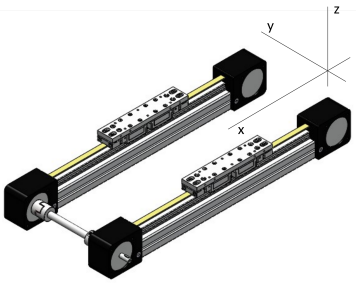

Figure 12. Configuration of the two linear actuators: 2x.

In order to make the system compact, the motor was positioned perpendicularly to the axis of the linear actuators. The transmission system between the motor shaft and the linear actuator shaft is accomplished using two pulleys and a belt, and the transmission between the two linear actuators is achieved through a synchronizing shaft of the OSL type, as shown in Figure 13.

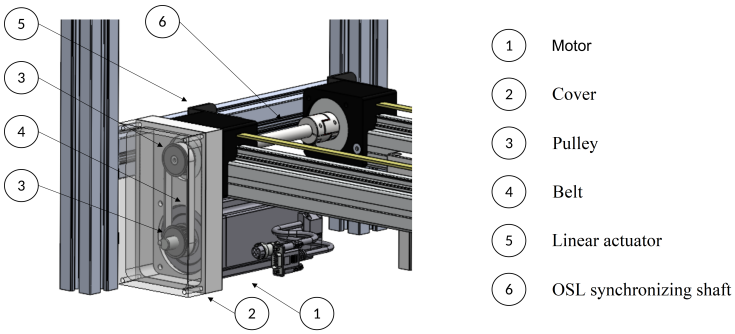

Figure 13. Components of the transmission system between the motor shaft and the linear actuator shaft and between the two shafts of the linear actuators.

3.8. Structural Configuration

The structural configuration of a machine is a crucial element for its performance and durability. It is necessary to consider the strength and stability of the structure to ensure that the machine can withstand the loads and vibrations to which it is subjected during operation. The 45 × 45 mm aluminum profiles represent an excellent balance between weight and strength, making them an ideal choice for such applications. These profiles have a square cross-section of 45 mm and are manufactured from a highly resistant aluminum alloy. Standard CAC anchor connectors and fasteners were employed to join the profiles. With external dimensions of 640 × 475 × 600 mm, as shown in Figure 14, the structure needs to accommodate the working area and the arms. To provide support and additional reinforcement, diagonal profiles have been added, as the machine will be subjected to high loads and vibrations during the process. This information is illustrated in Figure 15.

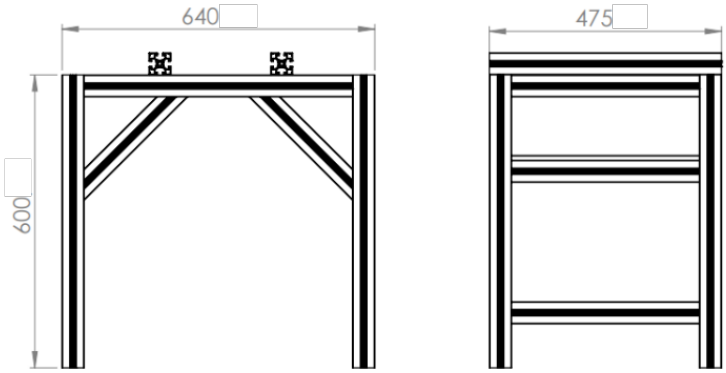

Figure 14. External dimensions of the structure.

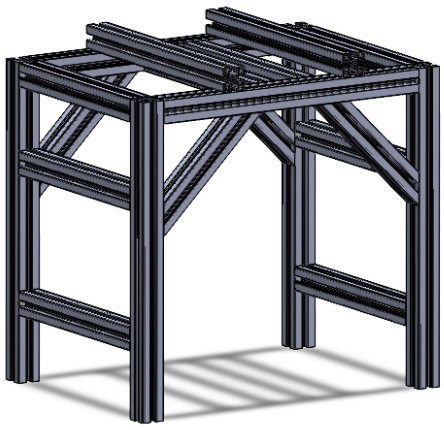

Figure 15. Projected view.

4. Simulations

The use of component and structure simulations enables the verification of the feasibility and performance of virtual designs, resulting in time and resource savings in the production process. SOLIDWORKS offers the possibility of performing static and dynamic simulations (with motion analysis), which are useful in different project situations. Static simulation is used to analyze the behavior of static models. It is useful for assessing the structural strength of parts and assemblies, as well as observing stresses and deformations under static conditions [25].

On the other hand, motion analysis simulation is used to analyze the behavior of a moving model, considering the forces and constraints that affect the motion of parts and assemblies. It helps evaluate the dynamics of mechanical systems, identify interferences, and optimize the performance of projects involving motion. The advantage of motion analysis over static simulation is that it provides features such as kinematic and dynamic analysis, force and torque calculations, and collision detection. These features can be used to simulate the effects of motion, including the influence of gravity, friction, and other physical phenomena, on parts and assemblies [25,26]. Motion analysis simulation allows for identifying potential issues in designs and making necessary changes before creating physical prototypes. In general, simulations using SOLIDWORKS, including static analysis and motion analysis, are a powerful tool for optimizing designs and improving product performance.

4.1. Motion Analysis Simulation

The simulations conducted took into account the forces acting on the tool tip and assumed that these forces are evenly distributed, with 3 kN in the vertical direction (z-axis) and 1 kN in both horizontal directions (x-axis and y-axis). Additionally, it was considered that the parts are made of EN10083:C45 steel, which is a type of medium-carbon construction steel. During the simulation, the tool holder and, consequently, the machine arms were moved to the critical locations of the workspace, which correspond to the four corners of the trapezoid, following the sequence shown in Figure 16 through the rotation provided by the motors. These critical points were verified when defining the machine's architecture.

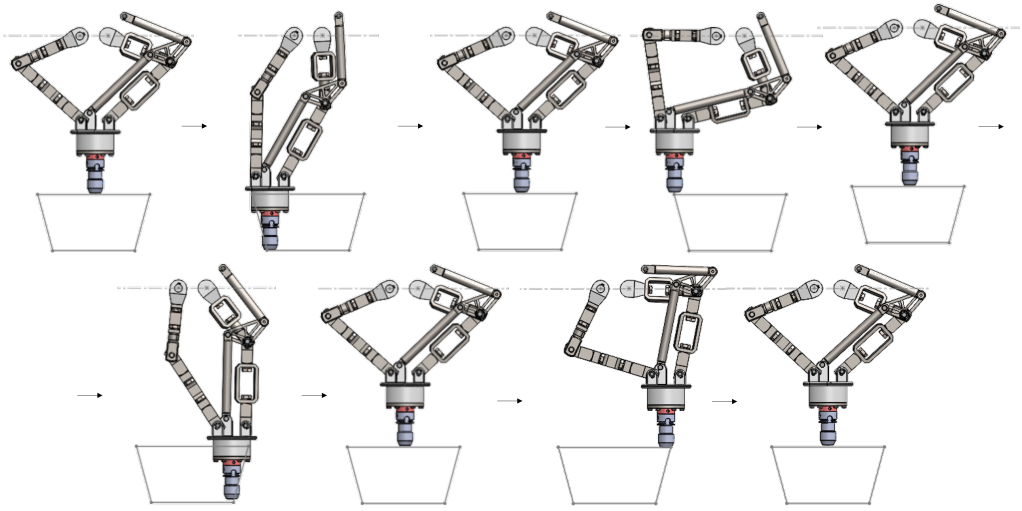

Figure 16. Sequence of the simulated robot's trajectory while passing through the critical points.

A study was conducted on the reaction force over the simulation time of potentially critical parts and connections. This computationally fast study allows for obtaining a graph with the curve of the reaction force over the simulation time, enabling a good initial analysis of critical efforts. After identifying the critical point on the workspace plane (peak of the curve), it is possible to simulate the component for a 0.2 s interval, consisting of 0.1 s before and 0.1 s after the specific point. A short simulation period was chosen to

avoid a significant increase in processing time. The main objective of this simulation is to evaluate the support capacity of the components against the stresses and forces they will be subjected to during operation and ensure that all connection components have a minimum safety factor of 1.5 in order to avoid any risk of failure or accidents. For this purpose, four main components were selected: the fork with pin, the universal coupler, the large parallel bar, and the platform. These components were considered critical due to their importance for the proper functioning of the machine and/or their exposure to higher stresses and forces. The simulations conducted allowed the evaluation of the results and the analysis of the viability of each component in relation to their specificities and requirements.

4.1.1. Component—Fork with Pin

The component called "fork with pin" is acquired in its final form of acquisition, and the main concern is ensuring that the force or stress to which this component is subjected does not exceed the specifications provided by the manufacturer. It is important to note that the component in question has different levels of stress on each side of the robot due to the asymmetry present in the device. Therefore, to ensure the proper functioning of the robot, it is crucial to examine both cases. Figure 17 shows the temporal variation in the exerted force and the position where it is maximum.

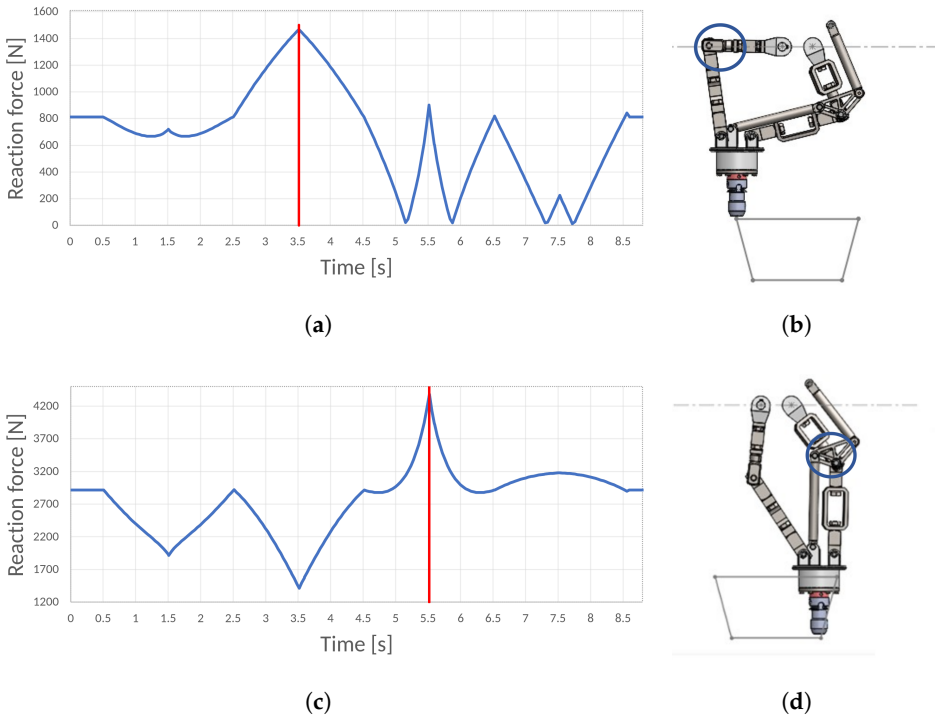

Figure 17. Graph of the reaction force over time on the "fork with pin" component on (**a**) the left side and on (**c**) the right side and the positions of the robot at the respective critical points in the (**b**) top-right corner and the (**d**) bottom-left corner. The red line points to the peak force.

From the analysis of the graph, it can be observed that the magnitude of the reaction force is lower on the left side compared to the right side, justified by the fact that the left side has two main arms while the right side has only one. Due to the higher reaction force on the right side, a simulation was performed at the critical position using a time interval from 5.4 to 5.6 s. The results are presented in Figure 18.

Given that the material used for the simulation is cold-drawn AISI 1045 construction steel with a yield strength of 530 MPa [27], it can be inferred that the adopted safety factor was 2. This value meets the minimum project requirement for a safety factor of 1.5, ensuring an adequate safety margin for the application at hand.

4.1.2. Component—Universal Coupler

The universal coupler is purchased as a finished product, and similar to the previous component, it is crucial to examine the component located on both the right side and left side of the robot to ensure proper functioning. Figure 19 presents graphs that illustrate the reaction force over time and the position of the robot at the respective critical points.

Upon analyzing the graphs, it is possible to observe a significant similarity between the graphs of the current component and the previous component (fork with pin). This similarity is a consequence of the simplification made during the simulation, in which all fixed parts were considered a rigid body. As a result, it can be concluded that the component has sufficient capacity to withstand the forces generated by the machine.

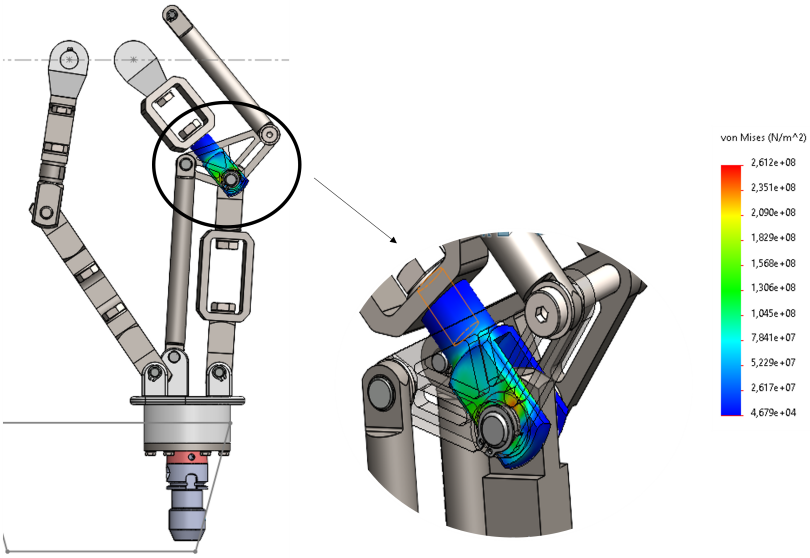

Figure 18. Simulation of the fork-with-pin component on the right side at the critical position.

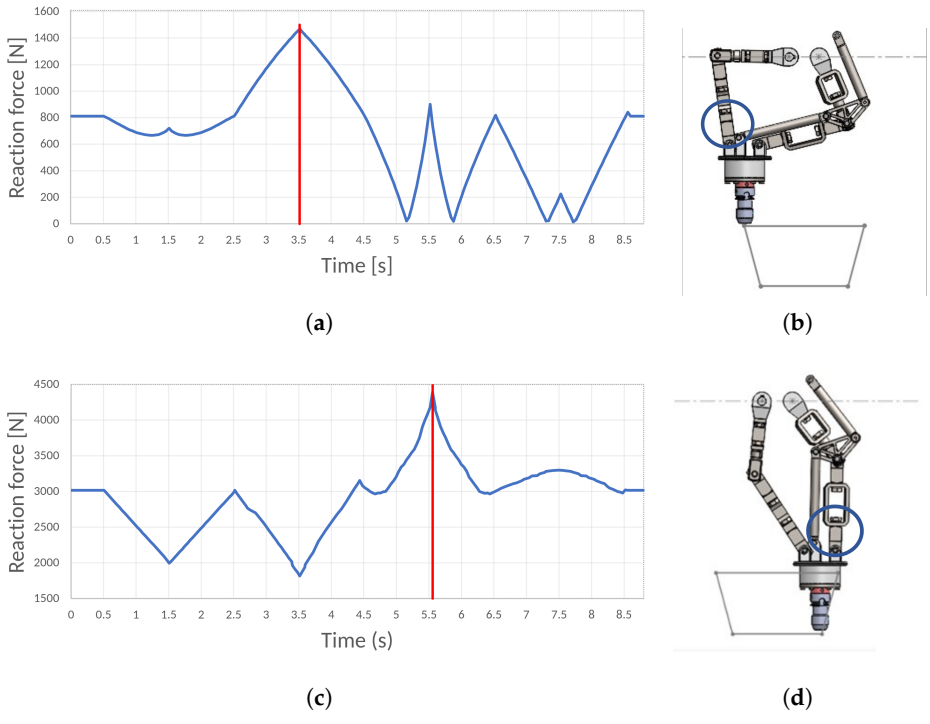

Figure 19. Graph of the reaction force over time on the universal coupler on (**a**) the left side and on (**c**) the right side and the positions of the robot at the respective critical points in the (**b**) top-right corner and the (**d**) bottom-left corner. The red line points to the peak force.

4.1.3. Component—Major Parallel Bar

An additional element of utmost importance for the project at hand is the major parallel bar, which will be manufactured internally. To ensure that the produced material is suitable for this application, it is crucial to determine the maximum stress that it will withstand. The analysis of the force reaction at the connection point with the platform over time is presented in Figure 20.

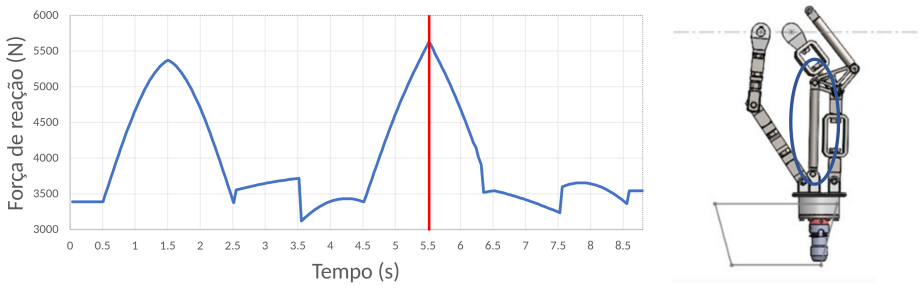

(**a**) (**b**)

Figure 20. Component—major parallel bar: (**a**) graph of the reaction force over time and (**b**) position of the robot at the respective critical point, lower-left corner. The red line points to the peak force.

Upon analyzing the graph, it can be observed that the maximum value of the reaction force is 5630 N. Considering that the bar in question has a circular shape with a diameter of 15 mm, we can apply Equation (35) to determine the maximum stress:

$$\sigma = \frac{F}{A} = \frac{F}{\pi \times r^2} \tag{35}$$

Based on this analysis, it can be concluded that the piece can be produced in aluminum since this material can withstand a stress of 33 MPa while maintaining a safety factor of 1.5.

4.1.4. Component—Platform

Another component to be produced is the platform. This piece is crucial for the operation of the machine. The potentially critical points are located at the connections with other components. Therefore, the reaction forces at these locations will be the same as those seen for the universal coupler and the large parallel bar components. With that being said, a simulation was performed during the time interval from 5.4 to 5.6 s, and the results are presented in Figure 21.

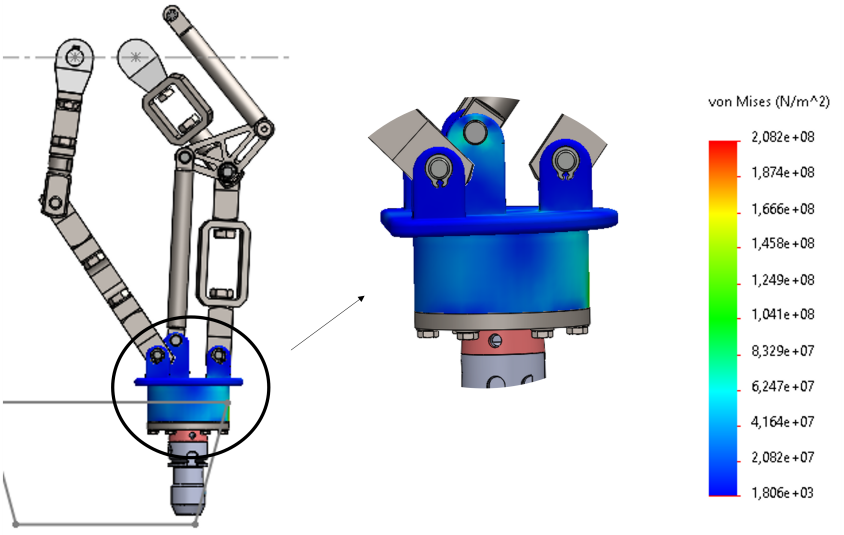

Figure 21. Simulation of the platform component in the critical position.

As expected, the safety factor of this component is greater than 1.5, ensuring an adequate safety margin for the specific application.

4.2. Static Simulation

A static analysis of the structure was adopted instead of a motion analysis simulation, as the structure exhibits predominantly static behavior. The analysis performed was linear, as it is simpler and faster than a non-linear analysis. A non-linear analysis is justified when there are large displacements, changes in the stiffness of the model, and non-linear stress–strain curves and when there is an influence on the order of load application. However, for this project, where the structure is kept within the elastic range and small displacements are expected, the results of the linear analysis are acceptable.

For pre-processing, boundary conditions, loadings, and simplifications were defined. The boundary conditions include fixing at the base. The loadings considered a 3 kN force in the vertical direction and 1 kN in both horizontal directions in the arm support zone and the loads from the reducer–motor in the reducer support zone. The simplifications include the elimination of unnecessary holes for the simulation. In Figure 22, the results of the static simulation can be visualized, showing variations in stress and deformation.

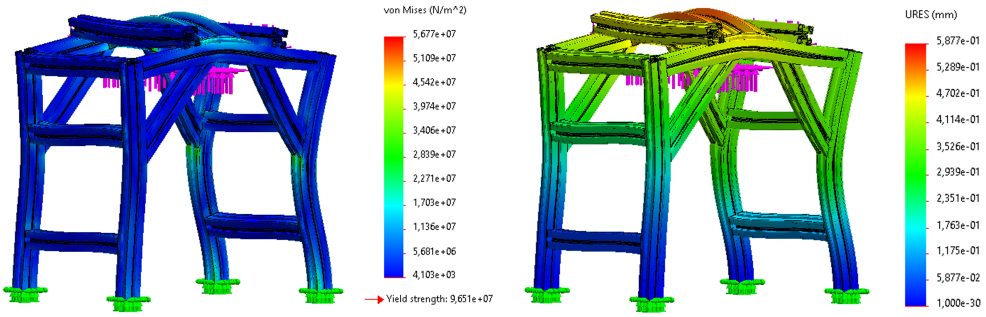

(**a**) (**b**)

Figure 22. Results of the static simulation of the structure for (**a**) stress and (**b**) displacement fields.

From the simulation results shown in Figure 22, it can be observed that most of the stresses occur in the connection zone between the vertical profile and the diagonal reinforcement profile. The largest displacements occur along the upper support profiles of the arms, reaching an amplitude of 0.59 mm. The safety factor is adequate for the project, with the critical point being above 1.3.

5. Conclusions

The SPIF process is an efficient and cost-effective solution for producing complex parts with different materials and scales. It surpasses conventional methods and is ideal for small series and customized products. SPIF can be implemented in various machines, such as adapted milling machines, serial robots, and dedicated machines, each with its own advantages. However, a dedicated SPIF machine offers superior performance, albeit requiring a higher initial investment. Integration between incremental forming and other processes such as 3D printing reduces the time to market and costs and offers greater design freedom. In an academic context, it is essential for the machine to be silent, compact, and electric to facilitate its coexistence with other machines.

In the design of the mechanical structure, the optimization of the robot arms was carried out, along with direct and inverse kinematic analysis. The design of the kinematic system to meet the initial requirement of always performing forming normal to the sheet surface required exhaustive research on solutions used in the industry for three-axis motion. Another requirement that had an impact on the design of the kinematic system was the workspace and the forces involved in the process. This led to the adoption of a D2 Delta robot for the y- and z-axes and linear actuators for the x-axis.

Other tasks included the design of the arms, the adaptation of components for the support system of the forming punch, and the selection and sizing of motors, reducers, and linear actuators. Simulations were also performed, and the structural configuration was developed. The design of the arms received special attention regarding the forces involved in the process. The selection of the various elements that make up the arms took into account the use of standardized elements and components that are easy to machine and assemble. Regarding the support system of the forming punch, it was necessary to have extensive practical knowledge in the field of machine tool design to develop a viable proposal. Once again, the main requirements to consider are the forces involved in the process and the use of standardized components. The selection and sizing of motors, gear reducers, and linear actuators proved to be fundamental aspects of the project, as they are responsible for the machine's motion and force.

Finally, the structure was designed to accommodate the arms and the workspace, allowing for the addition or integration of the remaining machine elements. In this case, a closed construction is more desirable, as the stability of the structure is more important than ideal accessibility to the workpiece. The current prototype developed (Figure 23) is believed to be a novel contribution regarding compact incremental forming machines, which will help disseminate the process to a larger audience, including rapid prototyping units, living side by side with 3D printers.

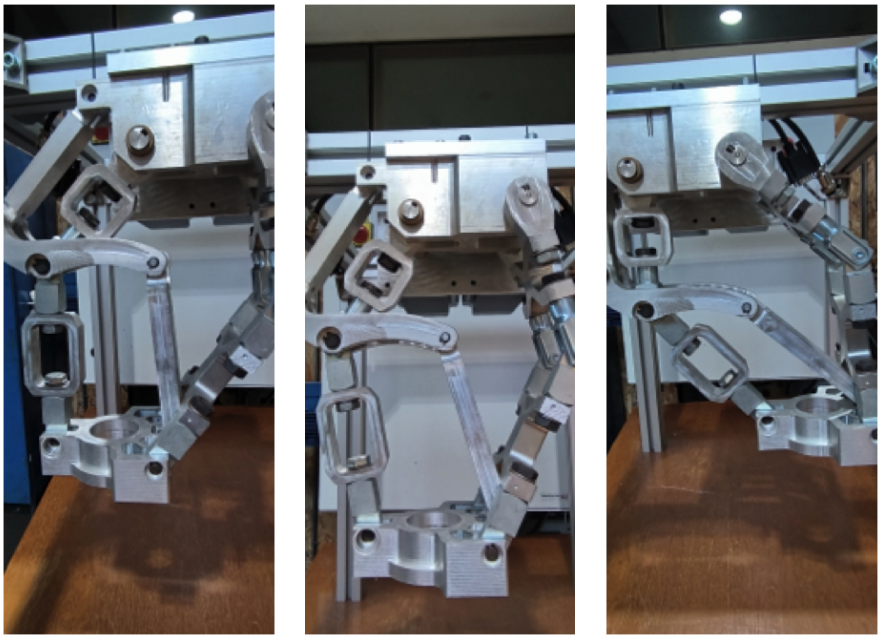

Figure 23. Prototype of the kinematic system.

Author Contributions: Conceptualization, D.G.A., R.J.A.d.S. and T.P.R.; methodology, D.G.A.; software, T.P.R.; validation, D.G.A., R.J.A.d.S. and T.P.R.; formal analysis, G.P.C.; investigation, T.P.R. and G.P.C.; resources, R.J.A.d.S.; writing—original draft preparation, G.P.C.; writing—review and editing, R.J.A.d.S.; visualization, D.G.A.; supervision, R.J.A.d.S.; funding acquisition, R.J.A.d.S. and D.G.A. All authors have read and agreed to the published version of the manuscript.

Funding: This work was supported by the projects UIDB/00481/2020 and UIDP/00481/2020—Fundação para a Ciência e a Tecnologia, DOI 10.54499/UIDB/00481/2020 (https://doi.org/10.54499/UIDB/00481/2020) and DOI 10.54499/UIDP/00481/2020 (https://doi.org/10.54499/UIDP/00481/2020).

Data Availability Statement: The full project files can be found at Tatiana Resende github, https://github.com/TatianaResend/SPIF-A_v2 (accessed on 15 January 2024).

Conflicts of Interest: The authors declare no conflict of interest.

References

1. Jeswiet, J.; Micari, F.; Hirt, G.; Bramley, A.; Duflou, J.; Allwood, J. Asymmetric single point incremental forming of sheet metal. *CIRP Ann. Manuf. Technol.* **2005**, *54*, 88–114. [CrossRef]
2. Duflou, J.R.; Habraken, A.M.; Cao, J.; Malhotra, R.; Bambach, M.; Adams, D.; Vanhove, H.; Mohammadi, A.; Jeswiet, J. Single point incremental forming: State-of-the-art and prospects. *Int. J. Mater. Form.* **2017**, *11*, 743–773. [CrossRef]
3. Afonso, D.; de Sousa, R.A.; Torcato, R. Integration of design rules and process modelling within SPIF technology—A review on the industrial dissemination of single point incremental forming. *Int. J. Adv. Manuf. Technol.* **2017**, *94*, 4387–4399. [CrossRef]
4. Jeswiet, J.; Hagan, E.; Szekeres, A. Forming parameters for incremental forming of aluminium alloy sheet metal. *Proc. Inst. Mech. Eng. Part B J. Eng. Manuf.* **2002**, *216*, 1367–1371. [CrossRef]
5. Emmens, W.; Sebastiani, G.; van den Boogaard, A. The technology of Incremental Sheet Forming—A brief review of the history. *J. Mater. Process. Technol.* **2010**, *210*, 981–997. [CrossRef]
6. Allwood, J.; Houghton, N.; Jackson, K. The Design of an Incremental Sheet Forming Machine. *Adv. Mater. Res.* **2005**, *6–8*, 471–478. [CrossRef]
7. Meier, H.; Dewald, O.; Zhang, J. Development of a Robot-Based Sheet Metal Forming Process. *Steel Res. Int.* **2005**, *76*, 167–170. [CrossRef]
8. Amino, M.; Mizoguchi, M.; Terauchi, Y.; Maki, T. Current Status of "Dieless" Amino's Incremental Forming. *Procedia Eng.* **2014**, *81*, 54–62. [CrossRef]
9. Marabuto, S.; Afonso, D.; Ferreira, J.; Melo, F.; Martins, M.A.; de Sousa, R.A. Finding the Best Machine for SPIF Operations—A Brief Discussion. *Key Eng. Mater.* **2011**, *473*, 861–868. [CrossRef]
10. Sousa, R.A.; Ferreira, J.A.; de Farias, J.B.S.; Torrão, J.M.N.; Afonso, D.; Martins, M. SPIF-A: On the development of a new concept of incremental forming machine. *Struct. Eng. Mech.* **2014**, *49*, 645–660. [CrossRef]
11. Bastos, R.P.; de Sousa, R.J.A.; Ferreira, J.A.F. Enhancing time efficiency on single point incremental forming processes. *Int. J. Mater. Form.* **2015**, *9*, 653–662. [CrossRef]
12. Yang, X.; Wang, S.; Dong, Y.; Yang, H. D2 Delta Robot Structural Design and Kinematics Analysis. *IOP Conf. Ser. Mater. Sci. Eng.* **2017**, *274*, 012009. [CrossRef]
13. Santos, V. *Robotica Industrial (Industrial Robotics)*; VDMA Services GmbH: Frankfurt, Germany, 2021; ISBN 979-8470370495.
14. SKF. NKIB 5906—Combined Needle-Roller Bearings. Available online: https://www.skf.com/pt/products/rolling-bearings/roller-bearings/needle-roller-bearings/combined-needle-roller-bearings/productid-NKIB%205906 (accessed on 15 March 2023).
15. Amastone. Tool Holders Types. Available online: https://toolholderexchange.com/tool-holders-101/ (accessed on 9 January 2023).
16. Sandes Blanes. HSK-A32-Porta Ferramentas Forma B (Weldon). Available online: https://sanchesblanes.com.br/busca?s=HSK-A32 (accessed on 14 April 2023).
17. Fernandes, J. *Project and Control of a Incremental Forming Machine*; University of Aveiro: Aveiro, Portugal, 2021. Available online: https://github.com/TatianaResend/SPIF-A_v2/blob/main/Ma%CC%81quina_Estampagem_Incremental_Compacta_JorgeFernandes_104580%5B6921%5D.pdf (accessed on 14 April 2023).
18. Nazzaro, J.; Hannifin, P.; Eitel, E. The Benefits of Gearboxes—and When to Pick Integrated Gearmotors. *MachineDesign*, 10 April 2013.
19. Russel, G. The Pros and Cons to Different Gear Motors. 2016. Available online: https://www.gordonrussell.com/articles-10-the-pros-and-cons-to-different-gear-motors# (accessed on 25 March 2023).
20. Tecnopower. Serie ABR. Available online: https://www.tecnopower.es/producto/serie-abr (accessed on 14 April 2023).
21. Tecnopower. Serie AER. Available online: https://www.tecnopower.es/producto/serie-aer (accessed on 15 April 2023).
22. Tecnopower. Serie AE. Available online: https://www.tecnopower.es/producto/serie-ae (accessed on 15 April 2023).
23. Romanishin, J.; Bern, J.M.; Rus, D. Self-Reconfiguring Robotic Gantries Powered by Modular Magnetic Lead Screws. In Proceedings of the 2022 International Conference on Robotics and Automation (ICRA), Philadelphia, PA, USA, 23–27 May 2022. [CrossRef]
24. Gastreich, W. What Is a Linear Motion Control? 2018. Available online: https://realpars.com/motion-control/ (accessed on 25 April 2023).
25. Sharma, A.; Thapa, S.; Goel, B.; Kumar, R.; Singh, T. Structural analysis and optimization of machine structure for the measurement of cutting force for wood. *Alex. Eng. J.* **2023**, *64*, 833–846. [CrossRef]
26. Nedelcu, D.; Nedeloni, M.D.; Daia, D. The kinematic and dynamic analysis of the crank mechanism with solidworks motion. In Proceedings of the 11th WSEAS International Conference on Signal Processing, Computational Geometry and Artificial Vision, Florence, Italy, 23–25 August 2011; Volume 2011, pp. 245–250.
27. World Material. ASTM SAE AISI 1045 Carbon Steel Material. Available online: https://www.theworldmaterial.com/astm-sae-aisi-1045-carbon-steel-material/ (accessed on 14 April 2023).